Star Formation Newsletter #337 1-7

大橋聡史（理研）

- 1. Filament rotation in the California L1482 cloud
- 2. Dust polarized emission observations of NGC 6334; BISTRO reveals the details of the complex but organized magnetic field structure of the high-mass star-forming hub filament network
- 3. Photodissociation Region Diagnostics Across Galactic Environments
- 4. Linear Stability Analysis of a Magnetic Rotating Disk with Ohmic Dissipation and Ambipolar Diffusion
- 5. The sonic scale revealed by the world’s largest supersonic turbulence simulation
- 6. Physical and chemical structure of the Serpens filament – fast formation and gravitydriven accretion
- 7. Water and Methanol Ice in L1544

Dust polarized emission observations of NGC 6334; BISTRO reveals the details of the complex but organized magnetic field structure of the high-mass star-forming hub-filament network

http://arxiv.org/abs/2012.13060v1

BISTRO collaboration - D. Arzoumanian et al.

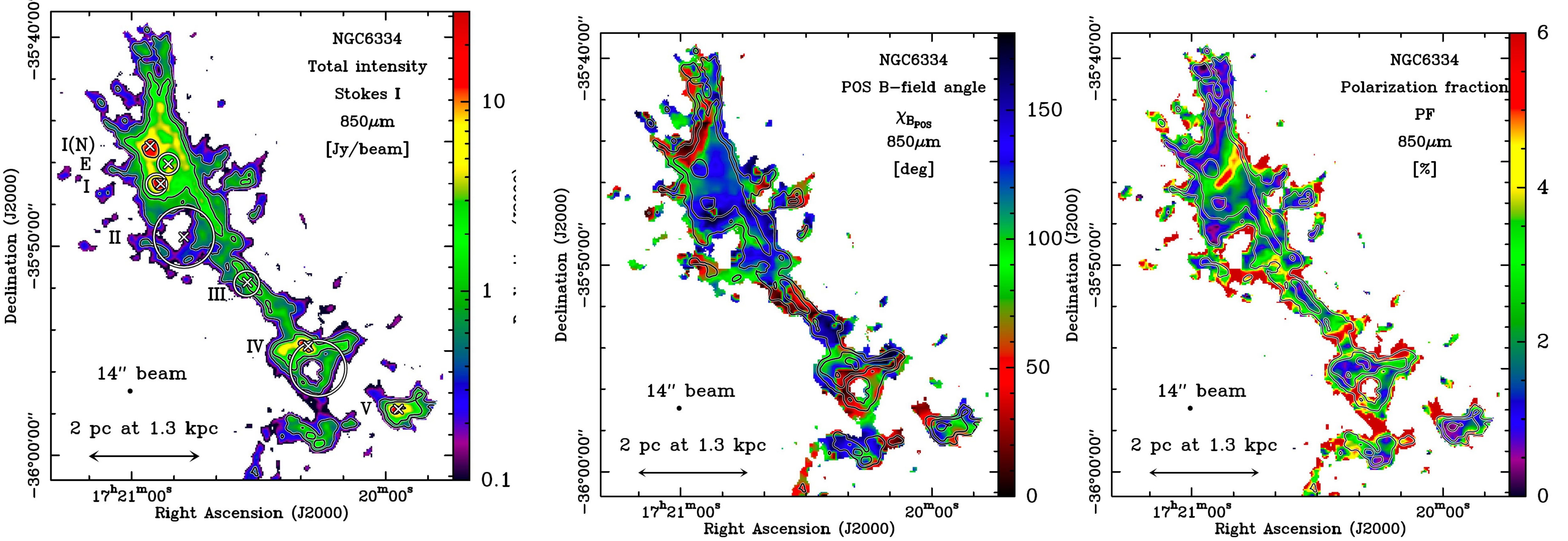

NGC 6334大質量星形成領域の偏光観測
→磁場の構造を0.07 pcで明らかにした

磁場に沿ってフィラメントが降着、hub領域では磁場と垂直

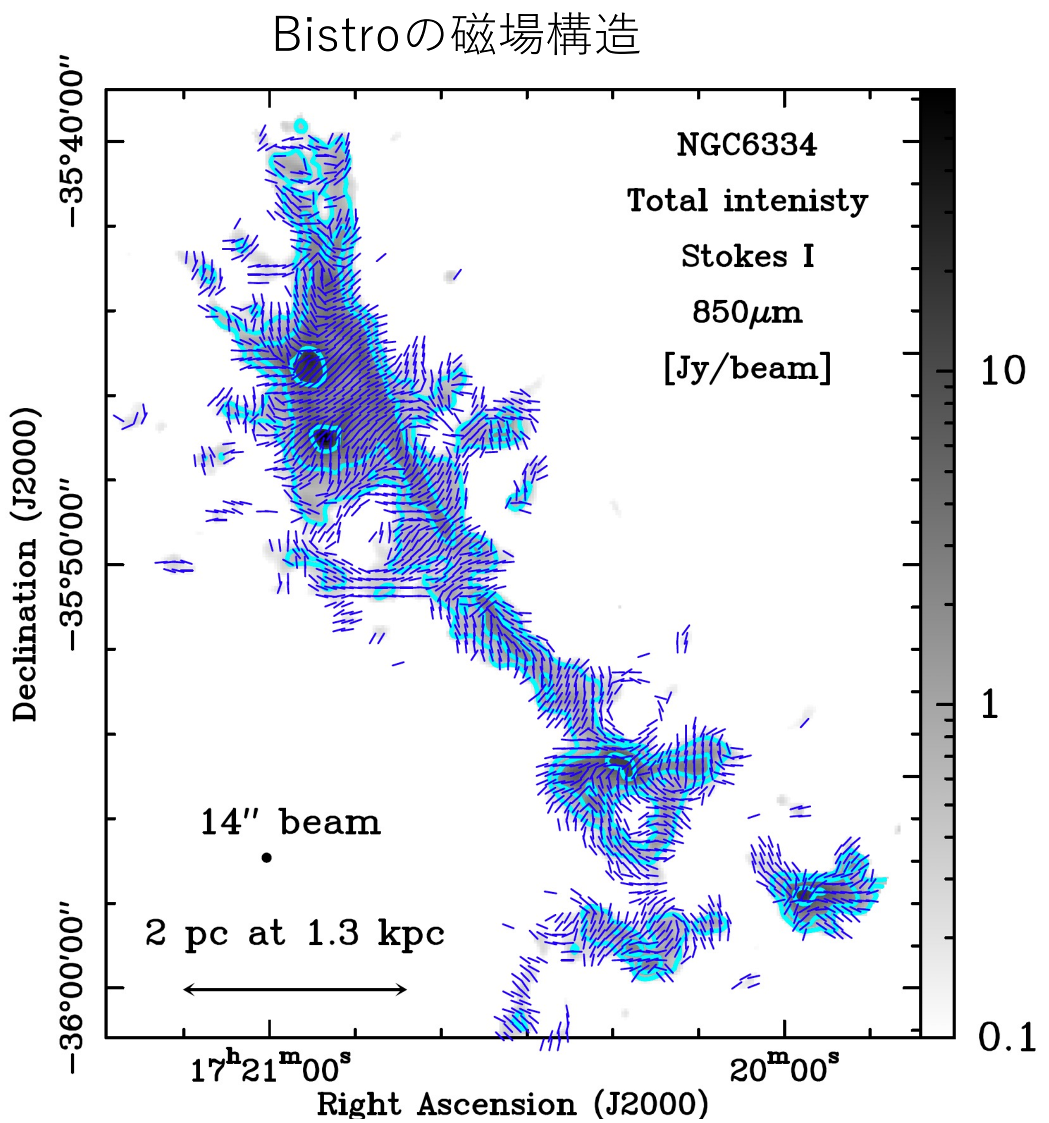

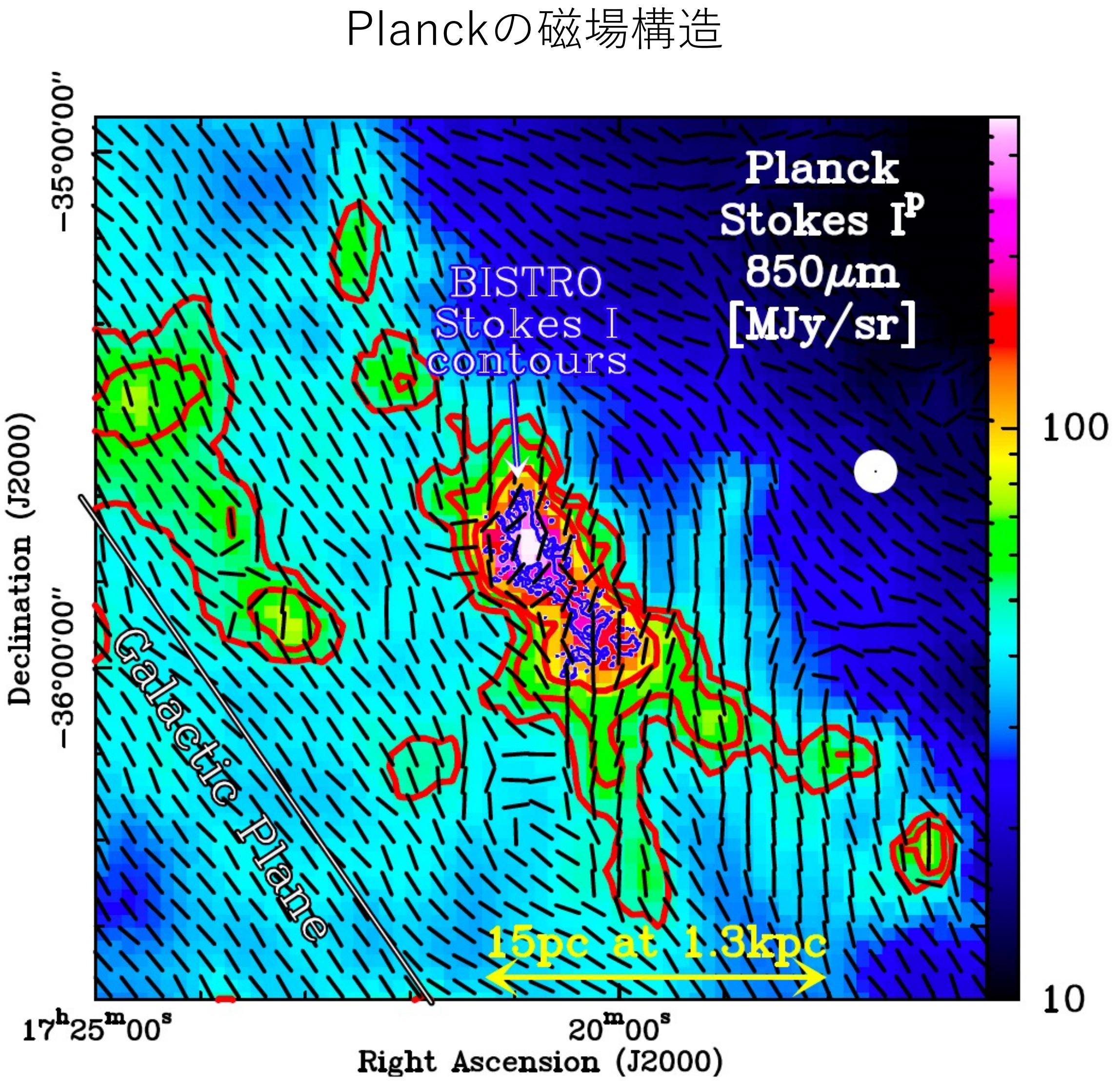

大きなスケールから構造が続いているが、コアスケールでは色々、
ただし、磁場ベクトルはwell ordered（scatterがあまりない）

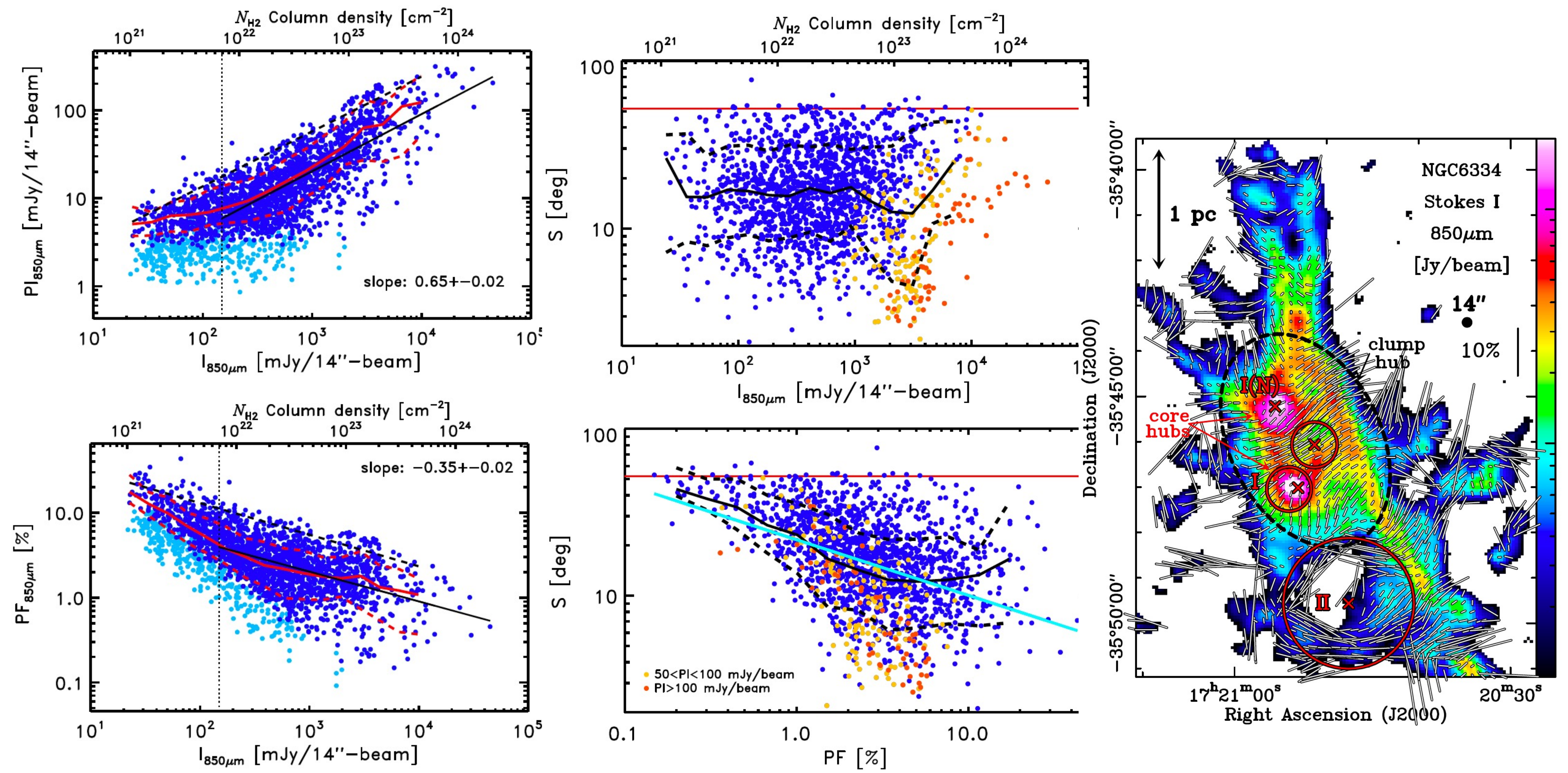

偏光度と強度にはpower law(-0.35)の関係、ただし、理論の予想とは違う。
ダストのアライメント効率やradiationの影響がありそう

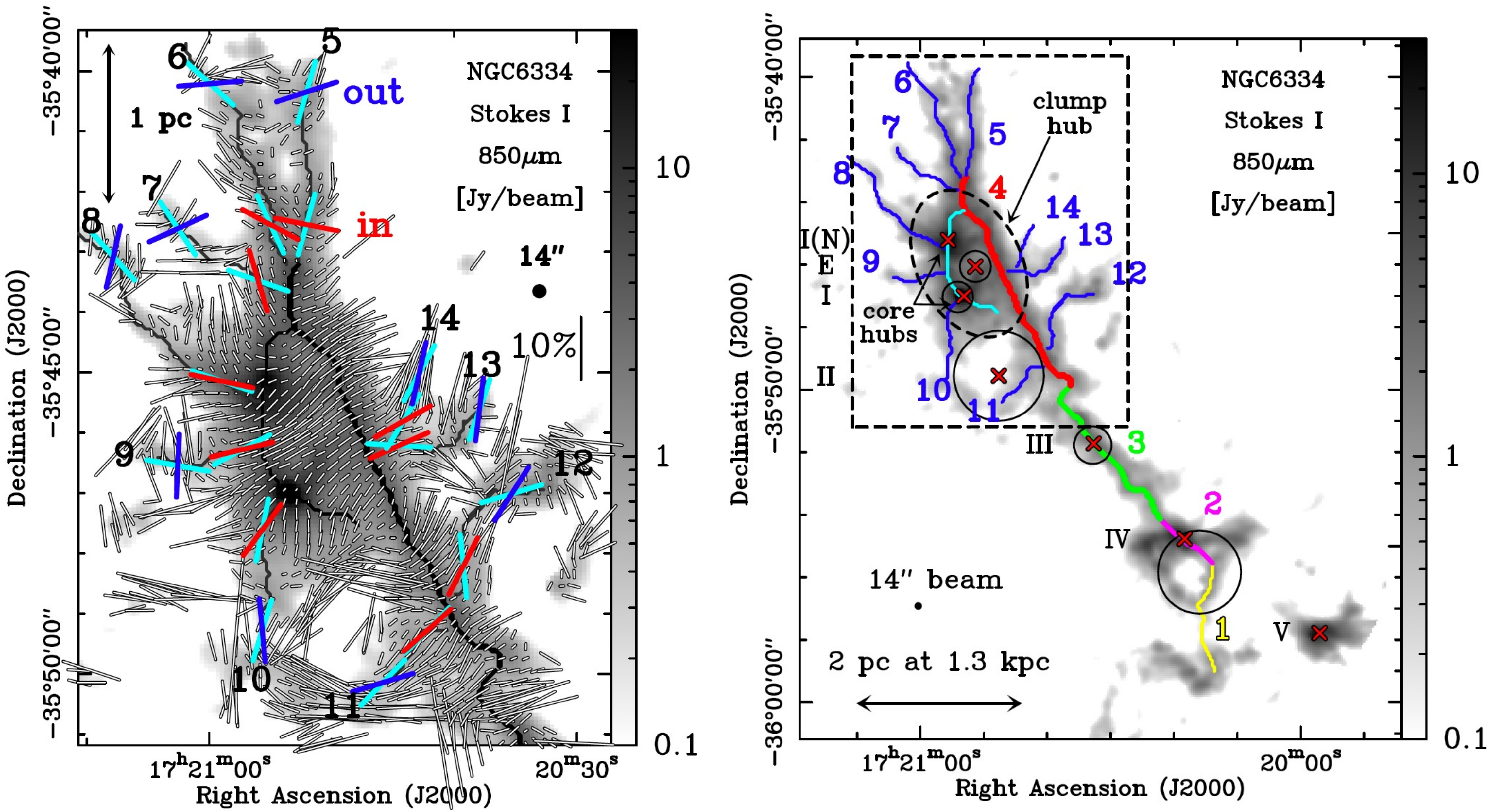

NGC6334
Stokes I
850μm
[Jy/beam]
1 pc
14″
10%
out
in
6
5
7
8
9
10
11
12
13
14
10
1
0.1
−35°40′00″
−35°45′00″
−35°50′00″
Declination (J2000)
17h21m00s
20m30s
Right Ascension (J2000)
clump hub
core hubs
I(N)
E
I
II
III
IV
V
1
2
3
4
14″ beam
2 pc at 1.3 kpc
−36°00′00″
20m00s

Crest # (1)	N_{H_2} [10^{23} cm^{-2}] (2)	n_{H_2} [10^5cm^{-3}] (3)	M_{line} [M$_\odot$/pc] (4)	σ_v [km/s] (5)	$M^v_{line,vir}$ [M$_\odot$/pc] (6)	B_{pos} [μG] (7)	$M^B_{line,crit}$ [M$_\odot$/pc] (8)	$M^{v,B}_{line,vir}$ [M$_\odot$/pc] (9)	α^T_{cyl} (10)	α^v_{vir} (11)	α^B_{vir} (12)	$\alpha^{v,B}_{vir}$ (13)
1	0.35 ± 0.21	1.0 ± 0.7	84 ± 60	0.40 ± 0.07	73 ± 26	101 ± 54	49 ± 32	123 ± 41	0.33 ± 0.25	0.9 ± 0.7	0.6 ± 0.6	1.5 ± 0.9
2	1.53 ± 1.21	4.5 ± 3.9	372 ± 325	0.63 ± 0.16	183 ± 95	585 ± 320	288 ± 189	471 ± 212	0.07 ± 0.07	0.5 ± 0.5	0.8 ± 0.8	1.3 ± 1.0
3	0.62 ± 0.18	1.8 ± 0.9	151 ± 70	0.47 ± 0.05	103 ± 19	144 ± 43	71 ± 33	175 ± 39	0.18 ± 0.10	0.7 ± 0.3	0.5 ± 0.3	1.2 ± 0.5
4	1.46 ± 0.33	4.3 ± 1.8	356 ± 152	0.62 ± 0.05	178 ± 27	818 ± 275	403 ± 199	581 ± 201	0.08 ± 0.04	0.5 ± 0.2	1.1 ± 0.7	1.6 ± 0.8
1 to 4	1.07 ± 0.52	3.1 ± 1.9	259 ± 158	0.56 ± 0.09	145 ± 45	270 ± 107	133 ± 71	278 ± 85	0.11 ± 0.07	0.6 ± 0.4	0.5 ± 0.4	1.1 ± 0.6
5 *in*	0.89 ± 0.10	2.6 ± 1.0	216 ± 82	0.53 ± 0.02	129 ± 11	139 ± 42	68 ± 32	198 ± 34	0.13 ± 0.06	0.6 ± 0.2	0.3 ± 0.2	0.9 ± 0.3
5 *out*	0.46 ± 0.03	1.3 ± 0.5	111 ± 41	0.43 ± 0.02	86 ± 7	71 ± 19	35 ± 16	121 ± 17	0.25 ± 0.11	0.8 ± 0.3	0.3 ± 0.2	1.1 ± 0.4
6 *in*	0.94 ± 0.10	2.8 ± 1.0	228 ± 86	0.54 ± 0.02	134 ± 11	203 ± 84	100 ± 55	234 ± 56	0.12 ± 0.05	0.6 ± 0.2	0.4 ± 0.3	1.0 ± 0.4
6 *out*	0.21 ± 0.11	0.6 ± 0.4	49 ± 32	0.34 ± 0.05	54 ± 16	32 ± 15	15 ± 9	70 ± 19	0.55 ± 0.38	1.1 ± 0.8	0.3 ± 0.3	1.4 ± 0.8
7 *in*	0.35 ± 0.28	1.0 ± 0.9	84 ± 74	0.40 ± 0.09	73 ± 34	227 ± 212	111 ± 112	185 ± 117	0.32 ± 0.30	0.9 ± 0.9	1.3 ± 1.8	2.2 ± 2.0
7 *out*	0.14 ± 0.03	0.4 ± 0.2	35 ± 14	0.32 ± 0.03	46 ± 8	32 ± 10	15 ± 7	61 ± 11	0.78 ± 0.38	1.3 ± 0.6	0.4 ± 0.3	1.8 ± 0.7
8 *in*	1.59 ± 0.71	4.7 ± 2.7	387 ± 223	0.64 ± 0.09	188 ± 55	277 ± 99	136 ± 70	325 ± 89	0.07 ± 0.04	0.5 ± 0.3	0.4 ± 0.3	0.8 ± 0.4
8 *out*	0.12 ± 0.03	0.4 ± 0.2	29 ± 13	0.30 ± 0.03	42 ± 8	38 ± 13	19 ± 9	61 ± 12	0.93 ± 0.47	1.4 ± 0.7	0.6 ± 0.4	2.1 ± 0.8
9 *in*	0.64 ± 0.27	1.9 ± 1.0	154 ± 86	0.48 ± 0.06	105 ± 28	495 ± 228	244 ± 143	349 ± 146	0.18 ± 0.11	0.7 ± 0.4	1.6 ± 1.3	2.3 ± 1.3
9 *out*	0.22 ± 0.03	0.7 ± 0.3	54 ± 20	0.35 ± 0.02	57 ± 7	63 ± 13	31 ± 13	89 ± 15	0.51 ± 0.23	1.1 ± 0.4	0.6 ± 0.3	1.6 ± 0.5
10 *in*	0.79 ± 0.39	2.3 ± 1.4	192 ± 117	0.51 ± 0.08	120 ± 37	351 ± 205	172 ± 119	293 ± 125	0.14 ± 0.09	0.6 ± 0.4	0.9 ± 0.8	1.5 ± 0.9
10 *out*	0.12 ± 0.04	0.4 ± 0.2	29 ± 14	0.30 ± 0.03	42 ± 9	18 ± 6	9 ± 4	51 ± 10	0.94 ± 0.51	1.4 ± 0.8	0.3 ± 0.2	1.8 ± 0.8
11 *in*	0.34 ± 0.05	1.0 ± 0.4	83 ± 32	0.40 ± 0.02	72 ± 8	109 ± 42	54 ± 28	126 ± 30	0.33 ± 0.15	0.9 ± 0.4	0.7 ± 0.4	1.5 ± 0.6
11 *out*	0.23 ± 0.06	0.7 ± 0.3	57 ± 25	0.36 ± 0.03	59 ± 11	80 ± 35	39 ± 22	98 ± 25	0.48 ± 0.25	1.0 ± 0.5	0.7 ± 0.5	1.7 ± 0.7
12 *in*	0.41 ± 0.06	1.2 ± 0.5	100 ± 39	0.42 ± 0.03	81 ± 9	208 ± 120	102 ± 70	184 ± 70	0.27 ± 0.13	0.8 ± 0.3	1.0 ± 0.8	1.8 ± 0.9
12 *out*	0.41 ± 0.10	1.2 ± 0.5	100 ± 44	0.42 ± 0.04	81 ± 13	105 ± 38	52 ± 26	133 ± 30	0.27 ± 0.14	0.8 ± 0.4	0.5 ± 0.4	1.3 ± 0.5
13 *in*	0.37 ± 0.11	1.1 ± 0.5	89 ± 42	0.40 ± 0.04	75 ± 15	158 ± 82	77 ± 49	153 ± 51	0.31 ± 0.17	0.8 ± 0.4	0.9 ± 0.7	1.7 ± 0.8
13 *out*	0.28 ± 0.05	0.8 ± 0.3	67 ± 27	0.37 ± 0.03	65 ± 9	40 ± 10	19 ± 8	84 ± 12	0.40 ± 0.19	1.0 ± 0.4	0.3 ± 0.2	1.2 ± 0.4
14 *in*	0.20 ± 0.05	0.6 ± 0.3	48 ± 21	0.34 ± 0.03	54 ± 9	61 ± 27	30 ± 17	84 ± 19	0.57 ± 0.28	1.1 ± 0.5	0.6 ± 0.4	1.7 ± 0.7
14 *out*	0.12 ± 0.04	0.3 ± 0.2	28 ± 13	0.30 ± 0.03	41 ± 9	89 ± 80	44 ± 42	85 ± 43	0.97 ± 0.53	1.5 ± 0.8	1.6 ± 1.7	3.0 ± 1.9
median *in*	0.64 ± 0.11	1.9 ± 1.0	154 ± 82	0.48 ± 0.04	105 ± 15	208 ± 99	102 ± 70	198 ± 70	0.27 ± 0.13	0.8 ± 0.4	0.9 ± 0.7	1.7 ± 0.8
median *out*	0.22 ± 0.04	0.7 ± 0.3	54 ± 25	0.35 ± 0.03	57 ± 9	63 ± 15	31 ± 13	85 ± 17	0.55 ± 0.38	1.1 ± 0.6	0.5 ± 0.3	1.7 ± 0.7

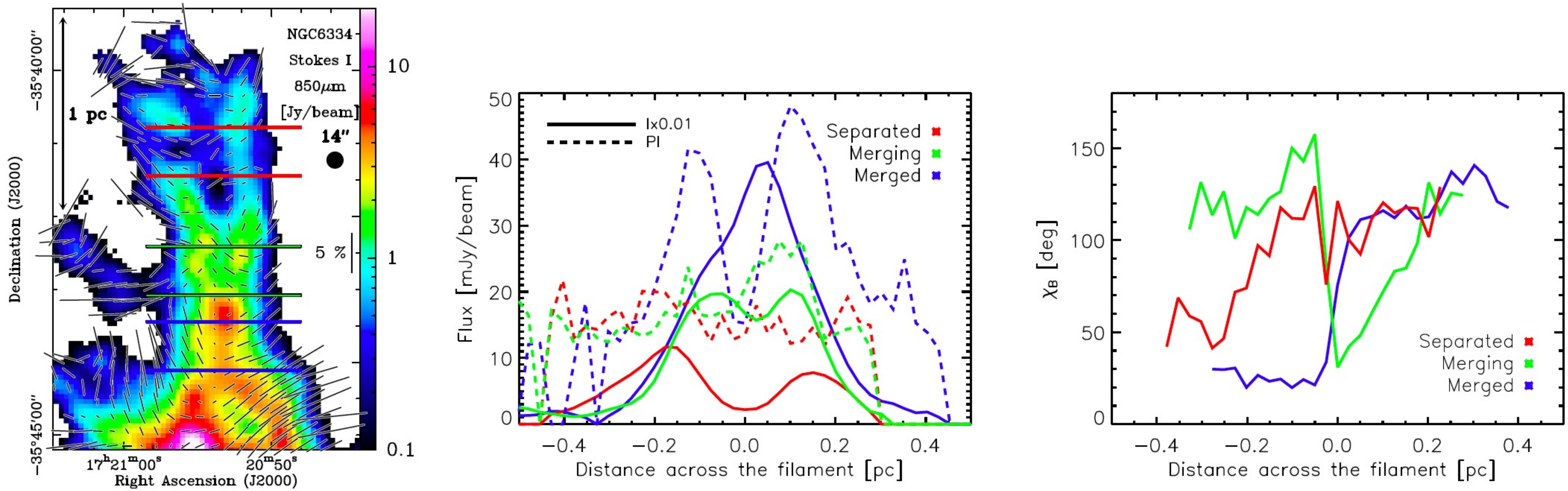

Converging flowフィラメントによってhubが形成、
磁場と垂直にフィラメントが作られ、重力によってねじ曲げられて、hubでは
磁場とフィラメントが平行になる。

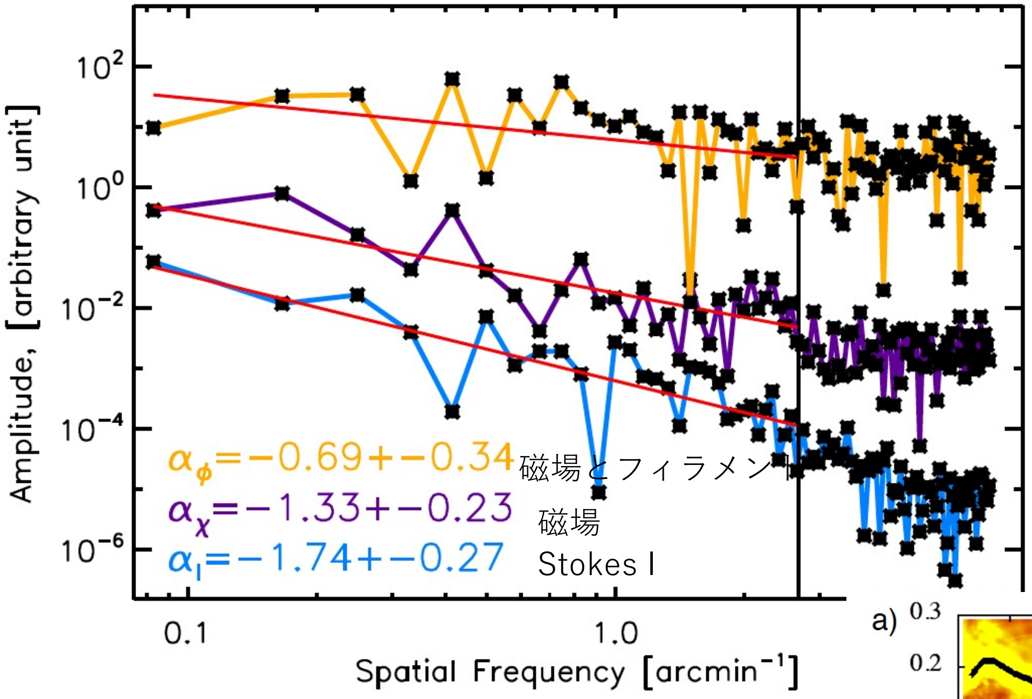

磁場と、フィラメント-磁場、Stokes Iのパワースペクトル
パワーローで説明できる、シミュレーションと一致

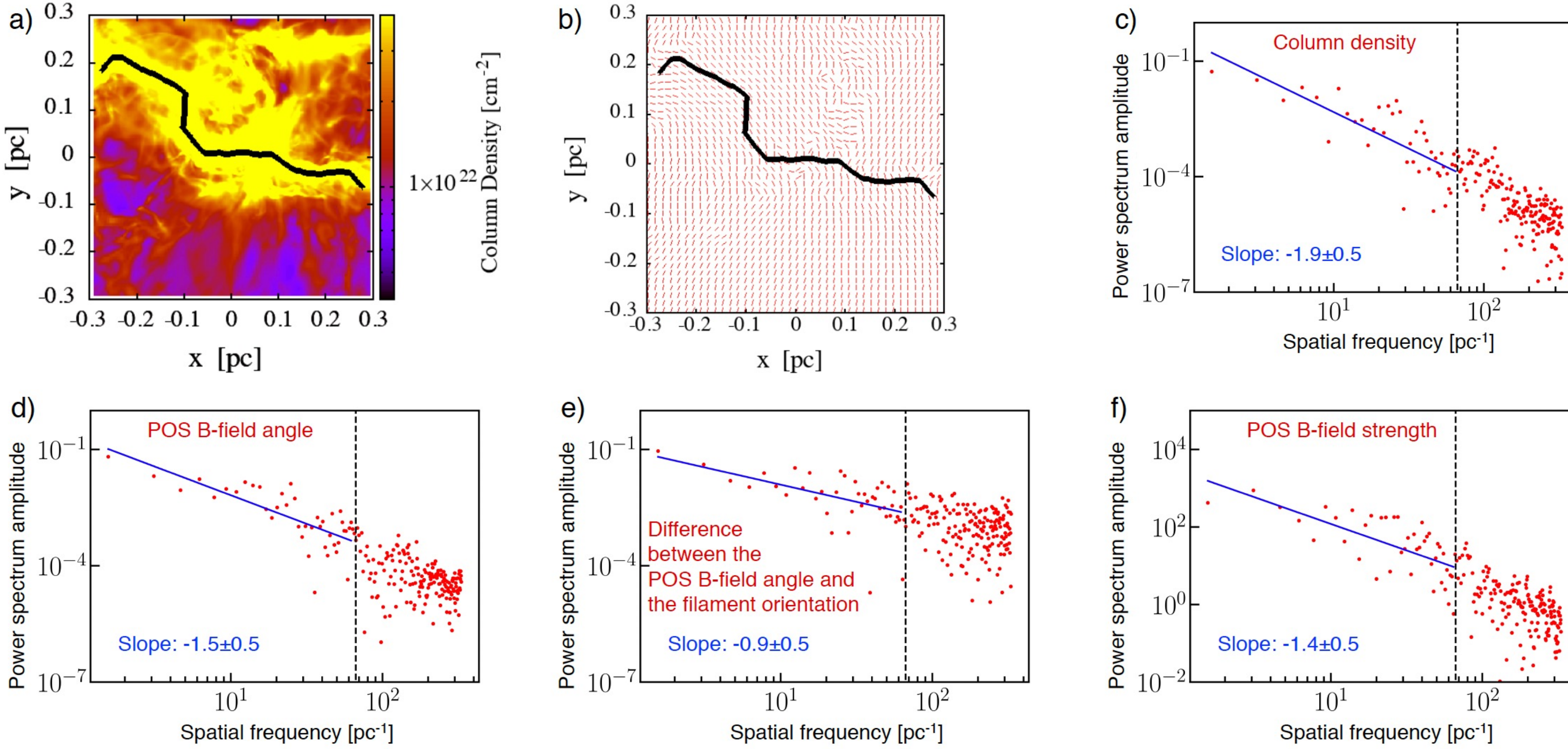

Physical and chemical structure of the Serpens filament – fast formation and gravity-driven accretion

Y. Gong, A. Belloche, F. J. Du, K. M. Menten, C. Henkel, G. X. Li, F. Wyrowski, R. Q. Mao The Serpens

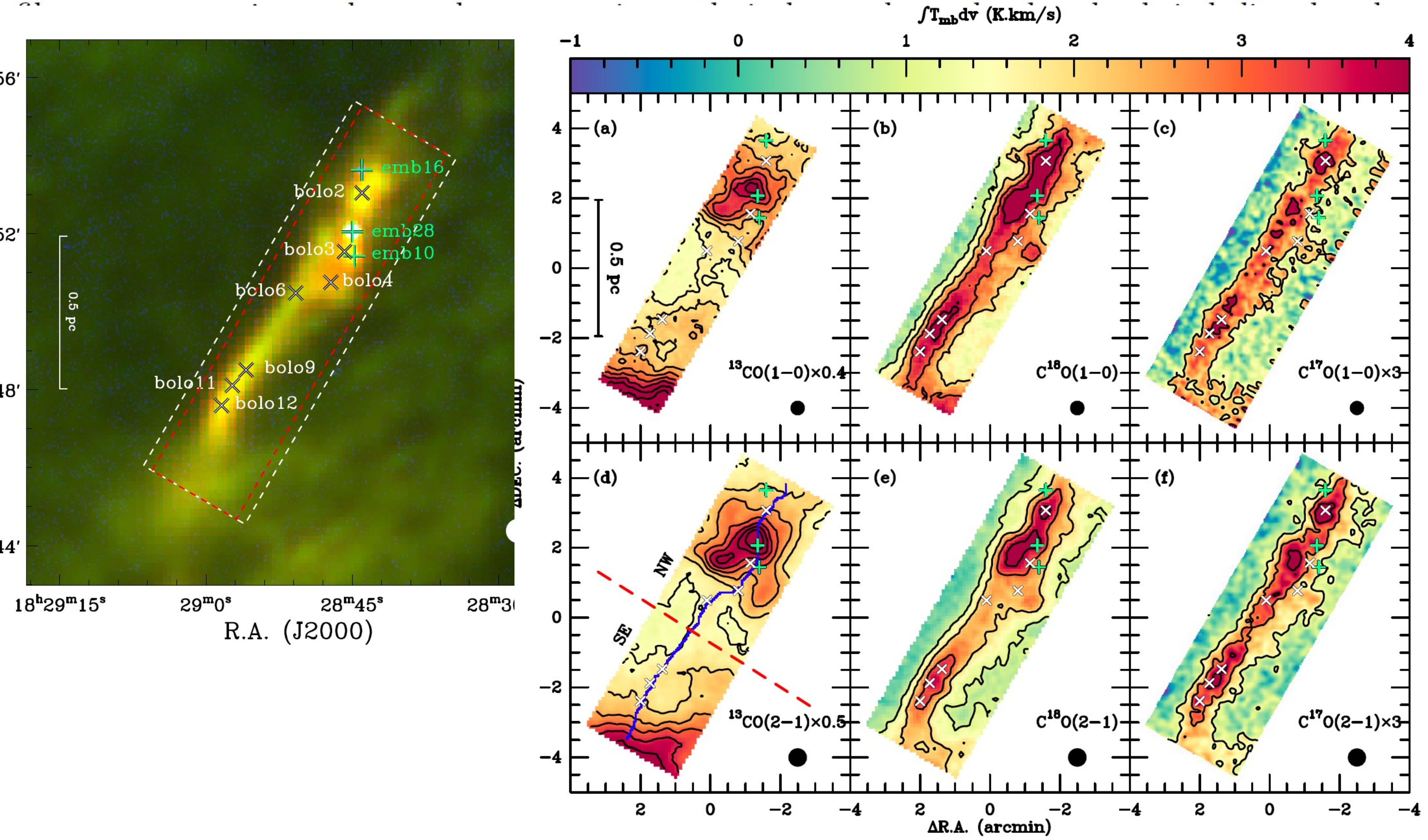

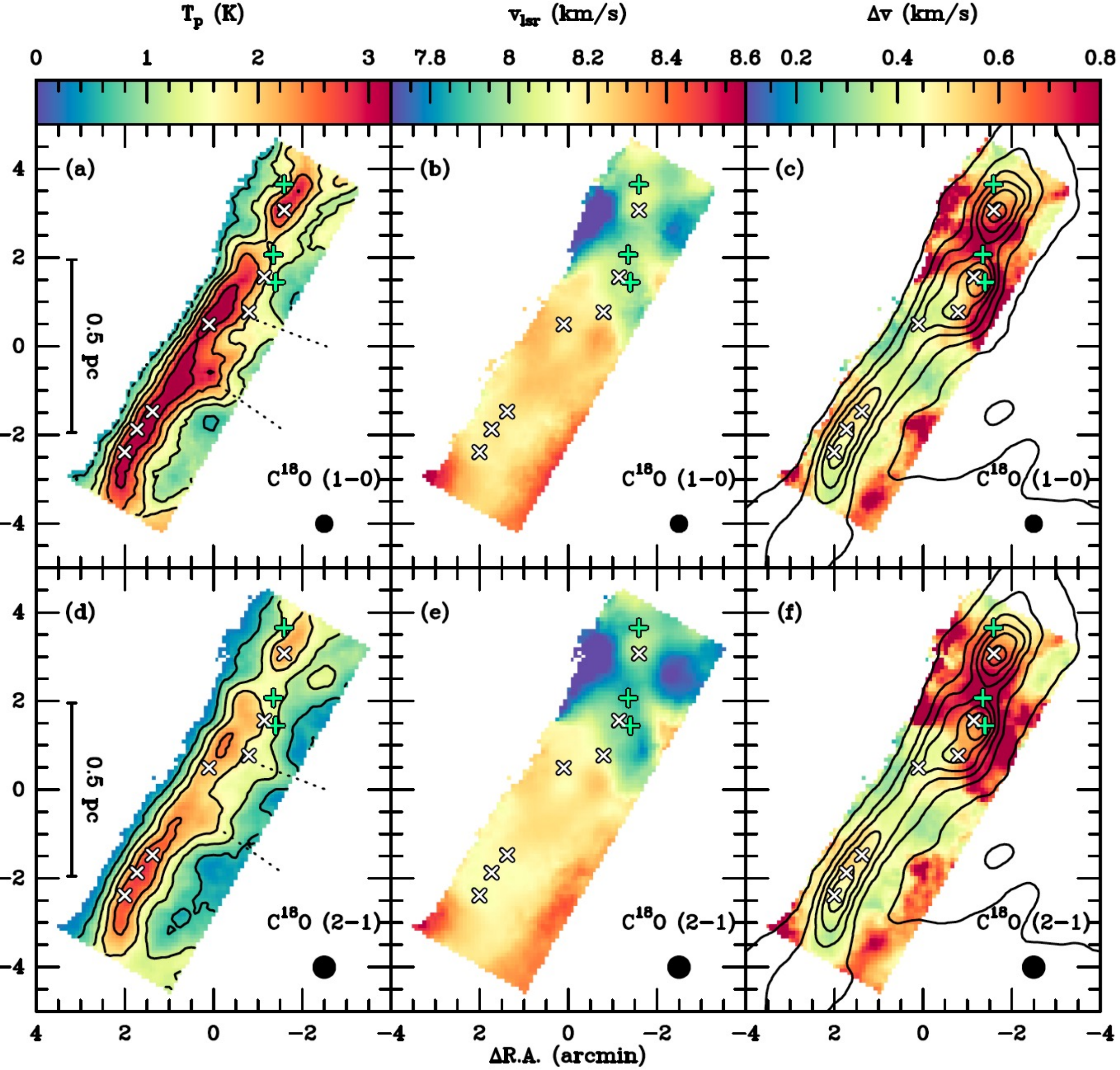

Tp (K)
vlsr (km/s)
Δv (km/s)
0.5 pc
(a)
(b)
(c)
(d)
(e)
(f)
C18O (1-0)
C18O (2-1)
ΔR.A. (arcmin)

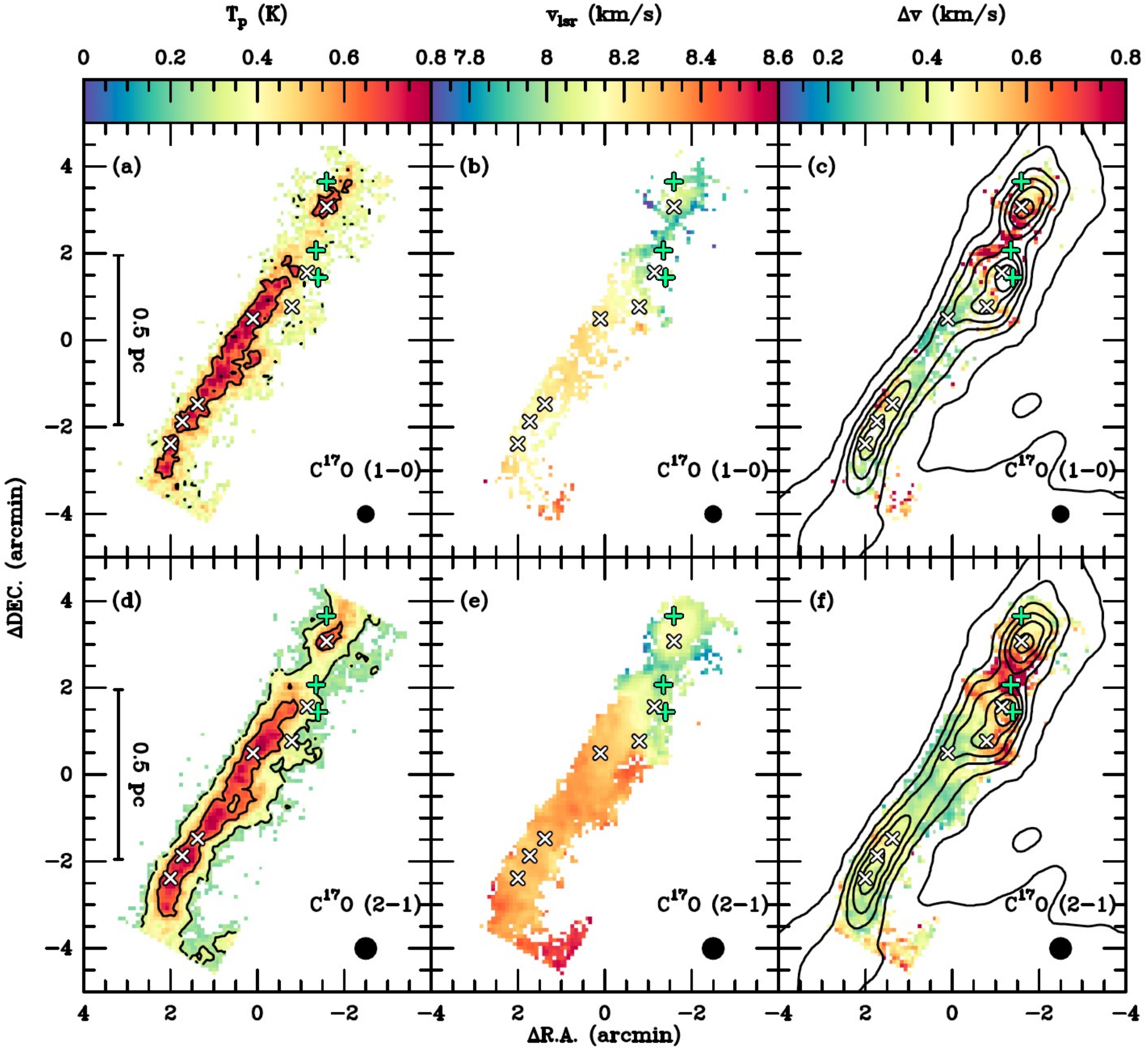

Tp (K)
vlsr (km/s)
Δv (km/s)
0.5 pc
(a)
(b)
(c)
(d)
(e)
(f)
C17O (1-0)
C17O (2-1)
ΔDEC. (arcmin)
ΔR.A. (arcmin)

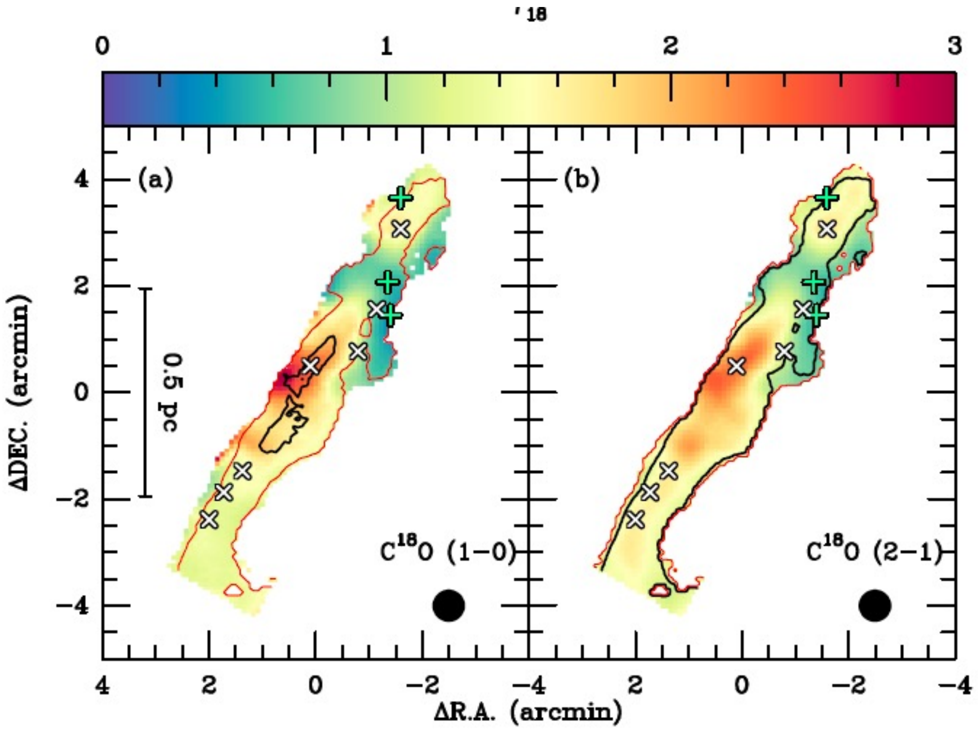

0
1
2
3
(a)
(b)
0.5 pc
ΔDEC. (arcmin)
ΔR.A. (arcmin)
C18O (1–0)
C18O (2–1)

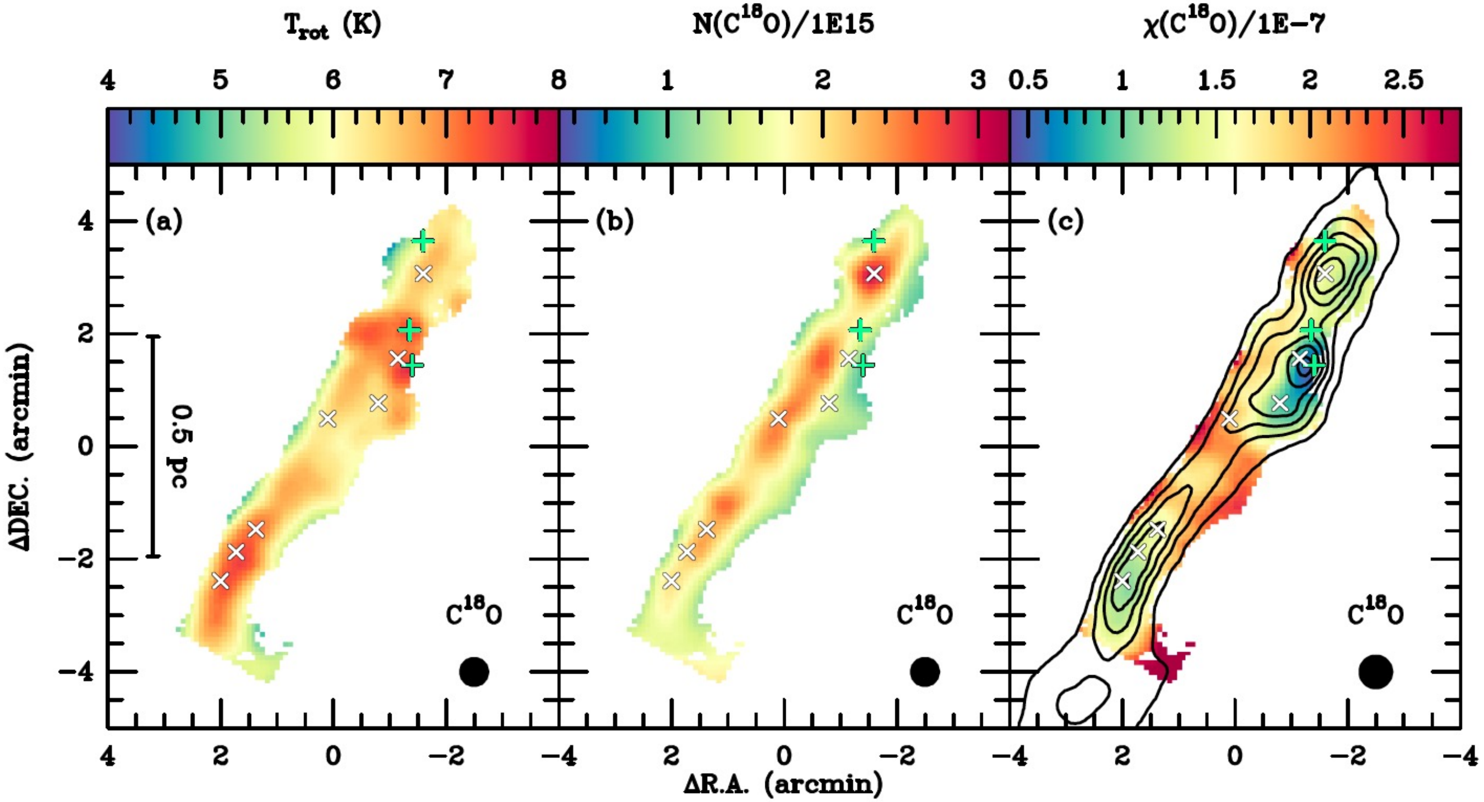

Trot (K)
N(C18O)/1E15
χ(C18O)/1E−7
(a)
(b)
(c)
0.5 pc
ΔDEC. (arcmin)
ΔR.A. (arcmin)
C18O

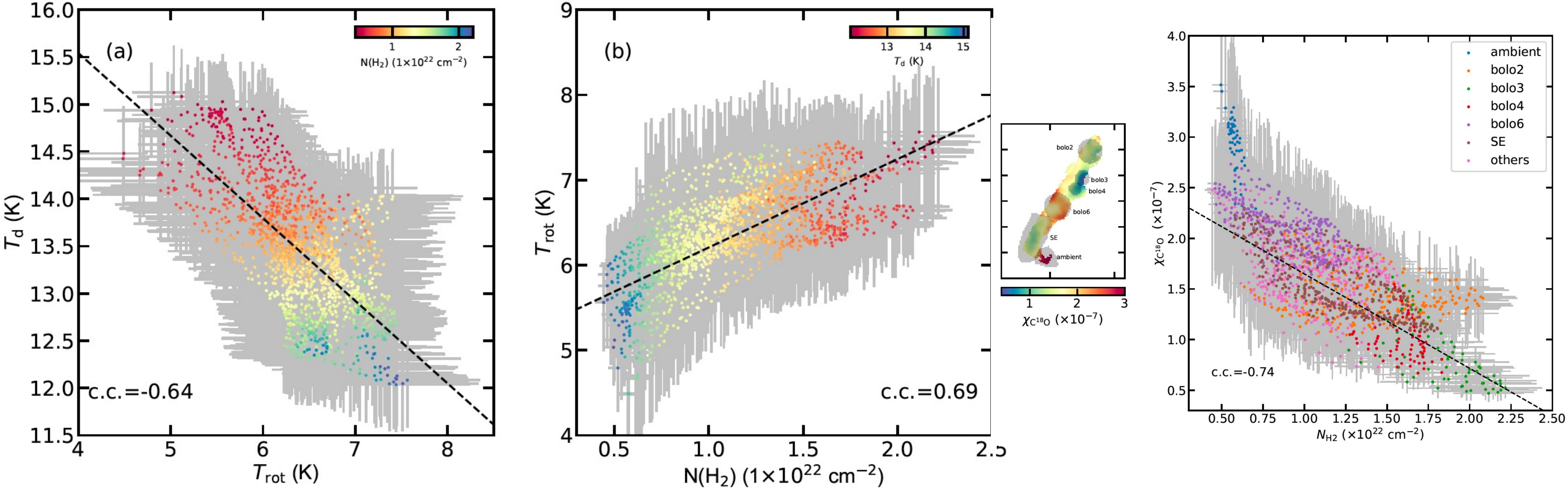

(a)
N(H₂) (1×10²² cm⁻²)
T_d (K)
T_{rot} (K)
c.c.=-0.64
(b)
T_d (K)
T_{rot} (K)
N(H₂) (1×10²² cm⁻²)
c.c.=0.69
bolo2
bolo3
bolo4
bolo6
SE
ambient
$\chi_{C^{18}O}$ (×10⁻⁷)
ambient
bolo2
bolo3
bolo4
bolo6
SE
others
$\chi_{C^{18}O}$ (×10⁻⁷)
N_{H2} (×10²² cm⁻²)
c.c.=-0.74

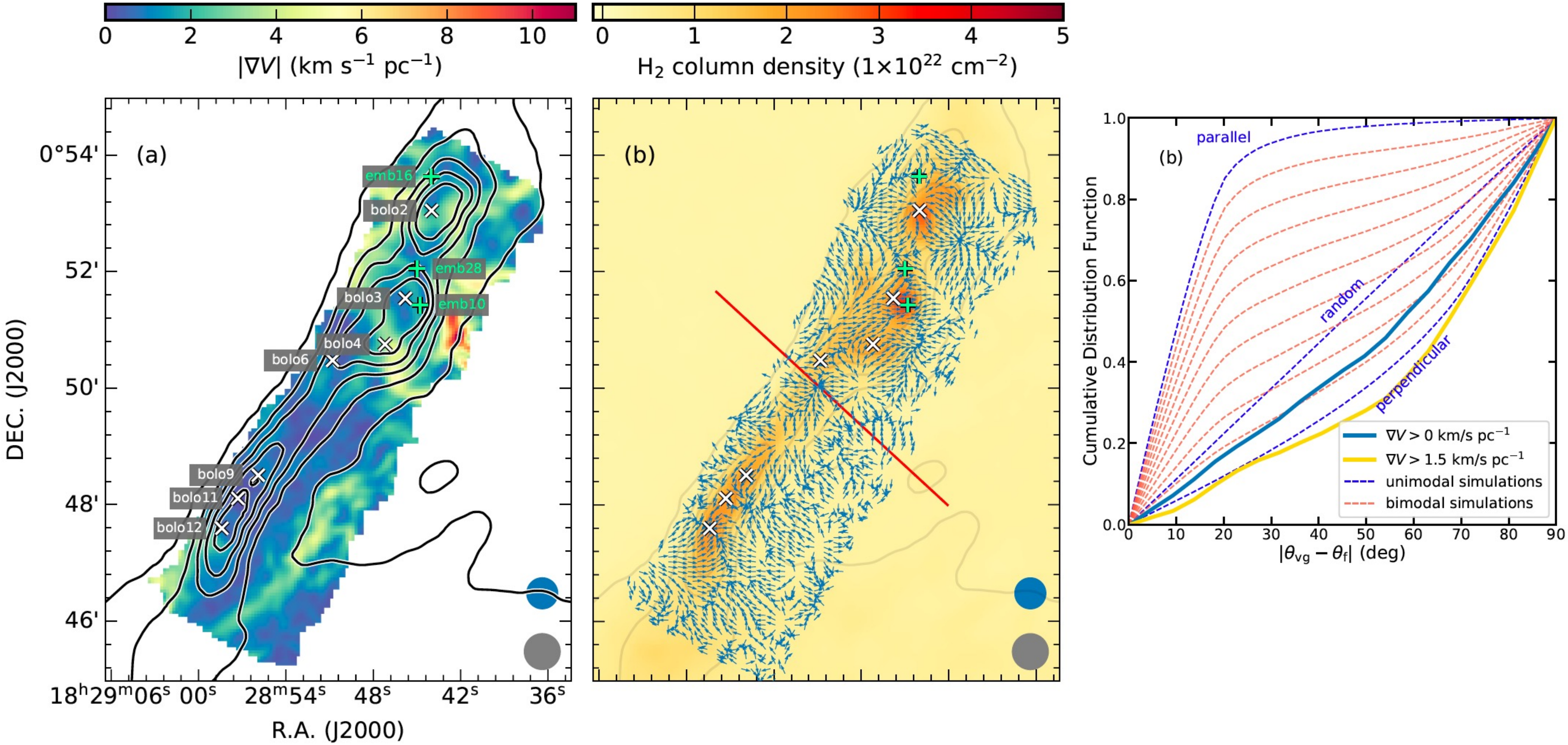

|∇V| (km s−1 pc−1)
0 2 4 6 8 10
H2 column density (1×10^22 cm−2)
0 1 2 3 4 5
(a)
(b)
emb16
bolo2
emb28
bolo3
emb10
bolo4
bolo6
bolo9
bolo11
bolo12
0°54'
52'
50'
48'
46'
DEC. (J2000)
18h29m06s 00s 28m54s 48s 42s 36s
R.A. (J2000)
Cumulative Distribution Function
parallel
random
perpendicular
∇V > 0 km/s pc−1
∇V > 1.5 km/s pc−1
unimodal simulations
bimodal simulations
|θvg − θf| (deg)

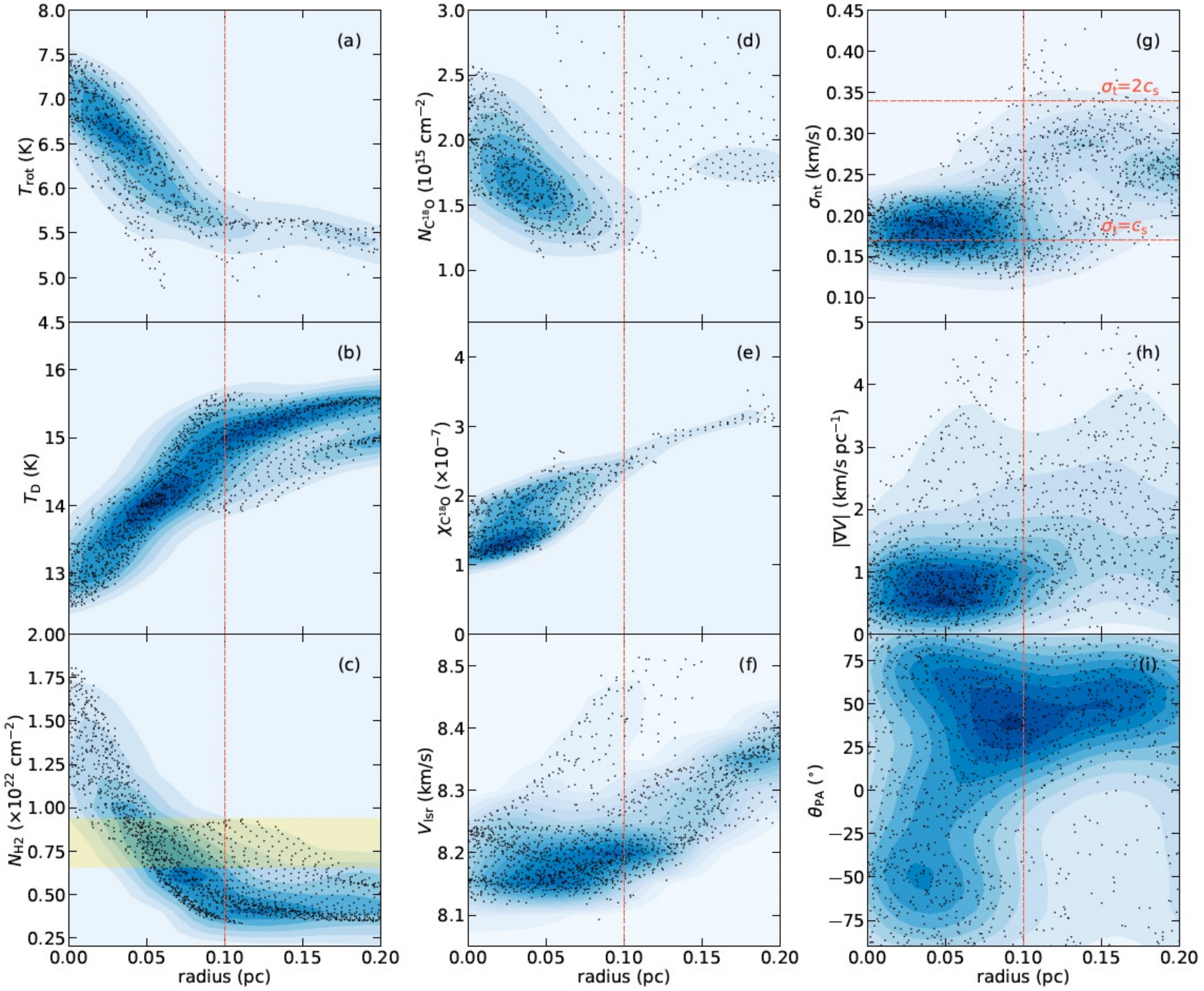
(a)
(b)
(c)
(d)
(e)
(f)
(g)
(h)
(i)
$T_{\rm rot}$ (K)
$T_{\rm D}$ (K)
$N_{\rm H2}$ ($\times 10^{22}$ cm^{-2})
$N_{\rm C^{18}O}$ (10^{15} cm^{-2})
$\chi_{\rm C^{18}O}$ ($\times 10^{-7}$)
$V_{\rm lsr}$ (km/s)
$\sigma_{\rm nt}$ (km/s)
$|\nabla V|$ (km/s pc^{-1})
$\theta_{\rm PA}$ (°)
$\sigma_{\rm t}=2c_{\rm s}$
$\sigma_{\rm t}=c_{\rm s}$
radius (pc)
radius (pc)
radius (pc)

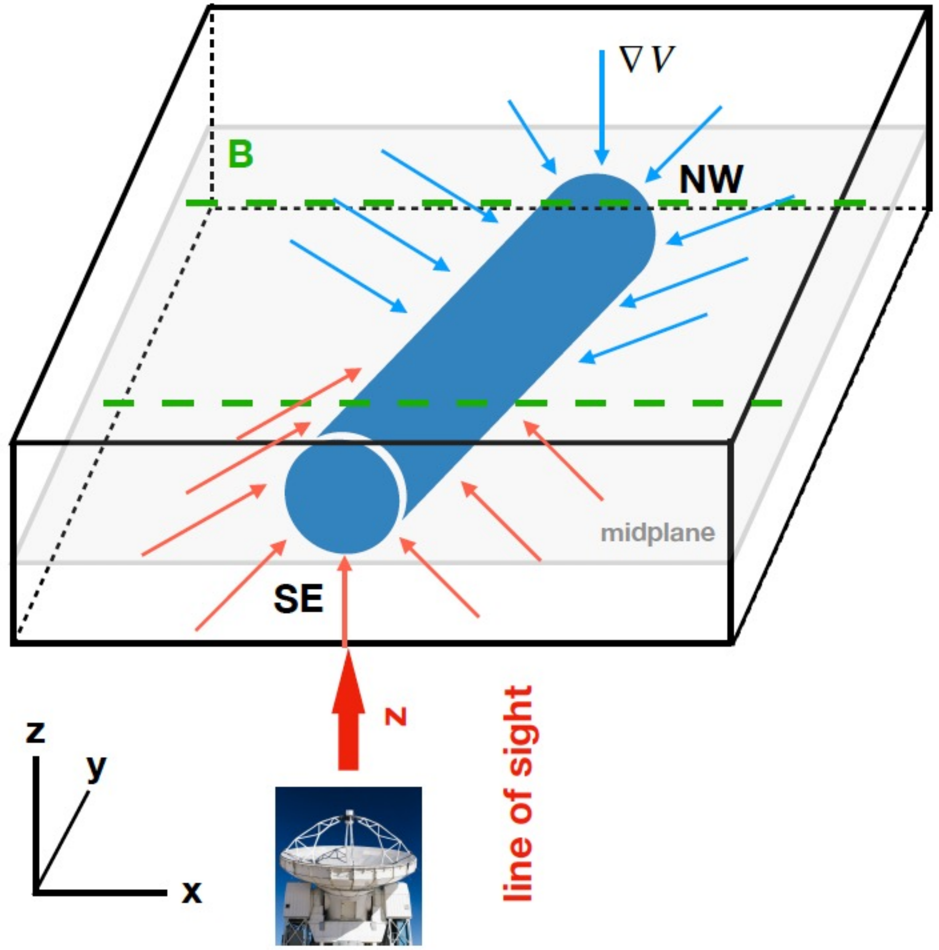
∇V
B
NW
SE
midplane
z
y
x
z
line of sight

Filament rotation in the California L1482 cloud

Rodrigo H. Álvarez-Gutiérrez, Amelia M. Stutz, Chi Y. Law, Stefan Reissl, Ralf S. Klessen, Nathan W. C. Leigh, Hong-Li Liu, Rodrigo A. Reeves We analyze the gas mass distribution, the gas kinematics, and the young stellar object (YSO) content of the California Molecular Cloud (CMC) L1482 filament. We derive a Gaia DR2 YSO distance of 511^{+17}_{-16} pc. We derive scale-free power-laws for the mean gas line-mass (M/L) profiles; we calculate the gravitational potential and field profiles consistent with these. We present IRAM 30 m $C^{18}O$ (1-0) (and other tracers) position-velocity (PV) diagrams that exhibit complex velocity twisting and turning structures. We find a rotational profile in $C^{18}O$ perpendicular to the southern filament ridgeline. The profile is regular, confined ($r \lesssim 0.4$ pc), anti-symmetric, and to first order linear with a break at $r \sim 0.25$ pc. The timescales of the inner (outer) gradients are ~0.7 (6.0) Myr. We show that the centripetal force, compared to gravity, increases toward the break; when the ratio of forces approaches unity, the profile turns over, just before filament breakup is achieved. The timescales and relative roles of gravity to rotation indicate that the structure is stable, long lived ($\sim$ a few times 6 Myr), and undergoing outside-in evolution. Moreover, this filament has practically no star formation, a perpendicular Planck plane-of-the-sky (POS) magnetic field morphology, and POS "zig-zag" morphology, which together with the rotation profile lead to the suggestion that the 3D shape is a corkscrew filament with a helical magnetic field. These results, combined with results in Orion and G035.39-00.33, suggest evolution toward higher densities as rotating filaments shed angular momentum. Thus, magnetic fields may be an essential feature of high-mass ($M \sim 10^5\ M_\odot$) cloud filament evolution toward cluster formation.

Photodissociation Region Diagnostics Across Galactic Environments

Thomas G. Bisbas, Jonathan C. Tan, Kei E. I. Tanaka We present three-dimensional astrochemical simulations and synthetic observations of magnetised, turbulent, self-gravitating molecular clouds. We explore various galactic interstellar medium environments, including cosmic-ray ionization rates in the range of $\zeta_{\rm CR} = 10^{-17}$-$10^{-14}\,{\rm s}^{-1}$, far-UV intensities in the range of $G_0 = 1$-10^3 and metallicities in the range of $Z = 0.1$-$2\,{\rm Z}_\odot$. The simulations also probe a range of densities and levels of turbulence, including cases where the gas has undergone recent compression due to cloud-cloud collisions. We examine: i) the column densities of carbon species across the cycle of CII, CI and CO, along with OI, in relation to the HI-to-H_2 transition; ii) the velocity-integrated emission of [CII] 158μm, [^{13}CII] 158μm, [CI] 609μm and 370μm, [OI] 63μm and 146μm, and of the first ten ^{12}CO rotational transitions; iii) the corresponding Spectral Line Energy Distributions; iv) the usage of [CII] and [OI] 63μm to describe the dynamical state of the clouds; v) the behavior of the most commonly used ratios between transitions of CO and [CI]; and vi) the conversion factors for using CO and CI as H_2-gas tracers. We find that enhanced cosmic-ray energy densities enhance all aforementioned line intensities. At low metallicities, the emission of [CII] is well connected with the H_2 column, making it a promising new H_2 tracer in metal-poor environments. The conversion factors of $X_{\rm CO}$ and $X_{\rm CI}$ depend on metallicity and the cosmic-ray ionization rate, but not on FUV intensity. In the era of ALMA, SOFIA and the forthcoming CCAT-prime telescope, our results can be used to understand better the behaviour of systems in a wide range of galactic and extragalactic environments.

Linear Stability Analysis of a Magnetic Rotating Disk with Ohmic Dissipation and Ambipolar Diffusion

Indrani Das, Shantanu Basu We perform a linear analysis of the stability of isothermal, rotating, magnetic, self-gravitating sheets that are weakly ionized. The magnetic field and rotation axis are perpendicular to the sheet. We include a self-consistent treatment of thermal pressure, gravitational, rotational, and magnetic (pressure and tension) forces together with two nonideal magnetohydrodynamic (MHD) effects (Ohmic dissipation and ambipolar diffusion) that are treated together for their influence on the properties of gravitational instability for a rotating sheet-like cloud or disk. Our results show that there is always a preferred lengthscale and associated minimum timescale for gravitational instability. We investigate their dependence on important dimensionless free parameters of the problem: the initial normalized mass-to-flux ratio μ_0, the rotational Toomre parameter Q, the dimensionless Ohmic diffusivity $\tilde{\eta}_{\mathrm{OD},0}$, and the dimensionless neutral-ion collision time $\tilde{\tau}_{\mathrm{ni},0}$ that is a measure of the ambipolar diffusivity. One consequence of $\tilde{\eta}_{\mathrm{OD},0}$ is that there is a maximum preferred lengthscale of instability that occurs in the transcritical ($\mu_0 \gtrsim 1$) regime, qualitatively similar to the effect of $\tilde{\tau}_{\mathrm{ni},0}$, but with quantitative differences. The addition of rotation leads to a generalized Toomre criterion (that includes a magnetic dependence) and modified lengthscales and timescales for collapse. When nonideal MHD effects are also included, the Toomre criterion reverts back to the hydrodynamic value. We apply our results to protostellar disk properties in the early embedded phase and find that the preferred scale of instability can significantly exceed the thermal (Jeans) scale and the peak preferred fragmentation mass is likely to be $\sim 10 - 90\ M_{\mathrm{Jup}}$.

The sonic scale revealed by the world's largest supersonic turbulence simulation

Christoph Federrath, Ralf S. Klessen, Luigi Iapichino, James R. Beattie Understanding the physics of turbulence is crucial for many applications, including weather, industry, and astrophysics. In the interstellar medium (ISM), supersonic turbulence plays a crucial role in controlling the gas density and velocity structure, and ultimately the birth of stars. Here we present a simulation of interstellar turbulence with a grid resolution of 10048^3 cells that allows us to determine the position and width of the sonic scale (l_s) - the transition from supersonic to subsonic turbulence. The simulation simultaneously resolves the supersonic and subsonic cascade, $v(l) \propto l^p$, where we measure $p_{sup} = 0.49$ +/- 0.01 and $p_{sub} = 0.39$ +/- 0.02, respectively. We find that l_s agrees with the relation l_s / L = phi$_s$ Mach$^{(-1/p_{sup})}$, where Mach is the three-dimensional Mach number, and L is either the driving scale of turbulence or the diameter of a molecular cloud. If L is the driving scale, we measure phi$_s$ = 0.42 (+0.12) (-0.09), primarily because of the separation between the driving scale and the start of the supersonic cascade. For a supersonic cascade extending beyond the cloud scale, we get phi$_s$ = 0.91 (+0.25) (-0.20). In both cases, phi$_s$ < 1, because we find that the supersonic cascade transitions smoothly to the subsonic cascade over a factor of 3 in scale, instead of a sharp transition. Our measurements provide quantitative input for turbulence-regulated models of filament structure and star formation in molecular clouds.

Water and Methanol Ice in L1544

Miwa Goto, A. I. Vasyunin, B. M. Giuliano, I. Jiménez-Serra, P. Caselli, C. G. Román-Zúñiga, J. Alves

Methanol and complex organic molecules have been found in cold starless cores, where a standard warm-up scenario would not work because of the absence of heat sources. A recent chemical model attributed the presence of methanol and large organics to the efficient chemical desorption and a class of neutral-neutral reactions that proceed fast at low temperatures in the gas phase. The model calls for a high abundance of methanol ice at the edge of the CO freeze-out zone in cold cloud cores. We performed medium resolution spectroscopy toward 3 field stars behind the starless core L1544 at 3 μm to constrain the methanol ice abundance and compare it with the model predictions. One of the field stars shows a methanol-ice abundance of 11% with respect to water ice. This is higher than the typical methanol abundance previously found in cold cloud cores (4%), but is 4.5 times smaller than predicted. The reason for the disagreement between the observations and the model calculations is not yet understood.